

Self-Supervised Curricular Deep Learning for Chest X-Ray Image Classification

Iván de Andrés Tamé
ivan.andrest@estudiante.uam.es

Kirill Sirotkin
kirill.sirotkin@uam.es

Pablo Carballeira
pablo.carballeira@uam.es

Marcos Escudero-Viñolo
marcos.escudero@uam.es

Video Processing and Understanding
Lab
Escuela Politécnica Superior
Universidad Autónoma de Madrid
28049 Madrid, Spain

Abstract

Deep learning technologies have already demonstrated a high potential to build diagnosis support systems from medical imaging data, such as Chest X-Ray images. However, the shortage of labeled data in the medical field represents one key obstacle to narrow down the performance gap with respect to applications in other image domains. In this work, we investigate the benefits of a curricular Self-Supervised Learning (SSL) pre-training scheme with respect to fully-supervised training regimes for pneumonia recognition on Chest X-Ray images of Covid-19 patients. We show that curricular SSL pre-training, which leverages unlabeled data, outperforms models trained from scratch, or pretrained on ImageNet, indicating the potential of performance gains by SSL pretraining on massive unlabeled datasets. Finally, we demonstrate that top-performing SSL-pretrained models show a higher degree of attention in the lung regions, embodying models that may be more robust to possible external confounding factors in the training datasets, identified by previous works [1, 2].

1 Introduction

The medical imaging field is constantly evolving, and solutions for diagnosis support systems, based on deep learning technologies bear many promises. However, even though the amount of collected medical data has never been larger, it is still (i) much smaller than in other application domains, (ii) often not publicly available and (iii) often not annotated. All these issues together impose significant constraints on the use of supervised deep learning solutions. Specifically, application scenarios for Chest X-Ray images (CXR) include [3]: classification and localization of pathologies, image segmentation to split the relevant region of the image to diagnose, and the generation of new synthetic images for data augmentation, or resolution increase.

Self-Supervised Learning Generally, the performance of supervised deep learning methods is directly related to the size of the labeled training dataset. This may harm its performance on CXR data, as the annotation of this data modality is a heavy burden that requires scarce and expensive expertise. Therefore, CXR data represent a paradigmatic modality for a current trend to improve the performance of visual tasks with a shortage of labeled data: Self-Supervised Learning (SSL) techniques. The hypothesis is that a combination of SSL pretraining on unlabeled data, followed by a fine-tuning step over the same target data can improve the performance of a model [25], as the SSL training aids to learn meaningful representations that act as an advantageous starting point for learning the target task.

For example in [16], it is claimed that by predicting relative locations of randomly sampled image patches the model learns high-level image representations. More recent works propose to learn efficient representations by matching the augmentations of the same image using the contrastive loss function. To avoid trivial solutions, SimCLR [7] uses very large batches during training increasing the number of negative samples. Momentum Contrast (MoCo) [27] introduces a memory queue that allows to decrease the batch size. Finally, BYOL [20] and SimSiam [9] rely only on positive pairs and propose other ways of preventing degenerate solutions, such as a momentum encoder and stop-gradient operations. Recent advances in SSL are closing the performance gap with the purely supervised models in natural imagining domains [6, 8, 10]. Moreover, SwAV [6] demonstrated that self-supervised features learned from ImageNet can outperform the supervised ones in transfer learning setups with Places205 [48], PASCAL VOC [17] and iNaturalist2018 [42] datasets. SSL pretraining has been assessed in several different medical domains. For instance, image-level diagnosis on CXR images has been explored in several works [18, 35]. Another study [28] proposed to use Rotation Prediction [19] and Jigsaw puzzles [62] to aid melanoma recognition on ISIC-2017 dataset, and more a recent work [33] investigates applications of DINO [6] to three standard medical imaging datasets: APTOS-2019 [26], ISIC-2019 [12] and CBIS-DDSM [30].

Some works have proposed to combine different pretext tasks to improve the performance of single-task SSL pretraining [15, 62, 41, 60]. The intuition behind combining pretext tasks is that different pretext tasks learn different visual representations from the same images [46], and thus, these different features contribute to a better representation of the data, and a better starting point for a downstream task. Doersch and Zisserman [15] combine four different SSL tasks at a batch level, i.e, each SSL task trains over the same batch before updating the network weights using a combination of the gradients. This strategy shows a performance improvement with respect to single-task pretraining on three datasets: ImageNet [27], PASCAL VOC [17], and NYU depth prediction [40]. In [41], Sirotkin *et al.* propose a curricular SSL pretraining method, where a CNN backbone is trained sequentially, using multiple SSL models. One of the main differences with respect to [15] is that this approach involves training on the complete dataset before changing the SSL task. This method is tested on the ISIC-2017 binary and ISIC-2019 multi-class skin lesion classification challenges [12, 43]. The authors provide evidence of performance improvement with respect to single-task pretraining, which depends on the ordering of pretraining pretext tasks.

In this work we explore the benefits of using a curricular SSL training scheme for pneumonia classification on CXR images of Covid-19 patients. We demonstrate that the best curricular-SSL pretraining achieves a balanced accuracy of 85.67%, which outperforms pretraining the model on ImageNet (82.75%) and random model initialization (83.69%).

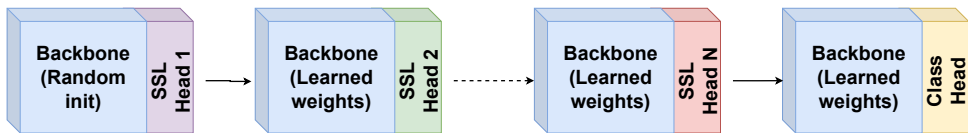


Figure 1: Curricular SSL training scheme, proposed in [41]. It uses a sequence of SSL tasks as a pretraining stage, and a final fine-tuning classification stage (downstream task).

Covid-19 pneumonia in CXR data Predominant findings of pneumonia in CXRs of Covid-19 patients are opacities inside the lung regions, which are defined as ground-glass opacities (GGO) [54, 47]. Empirical evidence [9] shows that radiologists themselves diagnose mainly based on the CXR data inside the lung regions. However, there are indications that recent deep learning systems targeting disease detection from CXRs, rather than learning on the medical pathology evidence, rely on confounding factors [44], out of the lung regions, as a learning shortcut. The confounding factors are prone to be dependent on the training dataset, so to avoid models that are overfitted to a given training dataset, and to increase the scalability and generalization capabilities of these solutions, there is a need to develop models that are robust to such confounding factors. One approach to indicate that a model is less affected by these external factors is the amount of attention it focuses on lung area.

In this work we propose a novel strategy to quantitatively compare different models in terms of the degree of attention they present in the lung regions. This strategy is used to show evidence that SSL pretraining (and curricular SSL pretraining) is beneficial to focus the model’s attention on the region of interest of the CXR image, in this case, the lungs. Therefore, SSL-pretrained models are prone to be more robust to the aforementioned external confounding factors.

2 Experimental design

2.1 Curricular SSL training scheme

We have used the curricular SSL training scheme proposed in [41] and depicted in Figure 1. The training pipeline is composed of N pretraining steps, each being an SSL task, and a final training on the downstream task, which in our work is a classification task. For all of the training steps we use the same backbone architecture, along with the same dataset. After each pretraining step, the backbone weights are transferred to the next step, making the model combine the learning from each SSL task to support the final classification. Training hyperparameters, e.g. learning rate or batch size, have a direct influence on the training pace and the final performance of a model. In a curricular SSL training, such as the one depicted on Figure 1, the hyper-parameters of each step may influence the subsequent ones. In this work, we have selected the learning-rate (LR) of each training step (both SSL steps and downstream classification) using the following policy:

- Each training step is repeated, using different LR values taken from a pre-defined range, for a limited number of epochs.
- The LR that leads to the highest performance (or lowest loss value) on the training task is used to train the model for the full number of epochs.

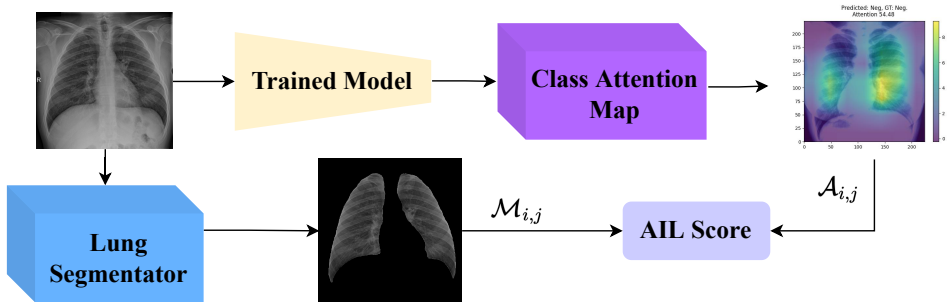


Figure 2: Overview of the processing scheme used to compute the AIL score. Note that, although we have included a lung texturized mask image (it allows to verify the correct lung segmentation), we use the binary segmentation mask computation of the AIL score.

2.2 Comparative analysis of the attention of the models: AIL Score

As detailed in Section 1, deep learning systems for pathology detection in CXRs may rely on confounding factors [14]. Moreover, other independent works [10, 11] demonstrate the same trend in the BIMCV-COVID19+ dataset—a part of the dataset used in this work (see details in Section 3). For the sake of scalability and utility, it is desirable to build models that focus their attention on the lung regions, ignoring the existence of external confounding factors in the training dataset. This presents an important advantage when the distribution of validation data differs from that of the training data. Specifically, if a model performs the classification prediction based on the data in the lung regions, it is prone to be more robust to background changes produced, for instance, by a change in the setup of a capturing device.

In this work, we investigate the degree of attention in the lung regions presented by models trained with different configurations of curricular SSL training schemes and fully-supervised ones. This is done through an attention score that measures the cumulative attention of a model with respect to the cumulative attention in the whole image: *Attention Inside the Lungs* (AIL, Equation 1). Figure 2 shows the processing scheme used to compute this AIL score. First, a Class Attention Map (CAM) [14] (predicted class), $\mathcal{A}_{i,j}$, is obtained from an input image and a model. Second, a binary mask of the lung regions, $\mathcal{M}_{i,j}$, is obtained using a state-of-the-art lung segmentation model. The AIL score is obtained as follows:

$$AIL = \frac{\sum_{i,j} \mathcal{A}_{i,j} \times \mathcal{M}_{i,j}}{\sum_{i,j} \mathcal{A}_{i,j}}. \quad (1)$$

The AIL score allows us to compare the level of attention of in-the-lung regions of several models. Higher AIL values correspond to CAMs with a higher focus in the lung regions.

In our implementation, lung segmentation has been carried out using the solution proposed by Selvan et al. [57], based on a U-net architecture and a variational encoder for data imputation, trained on public datasets labeled for tuberculosis detection [24], and specifically the model provided by the authors¹. The segmentation masks are post-processed using connected component analysis to exclude small erroneous regions and binary morphological closing to fill any small holes in the masks (see Figure 3 for examples).

¹https://github.com/raghavian/lungVAE/tree/master/saved_models

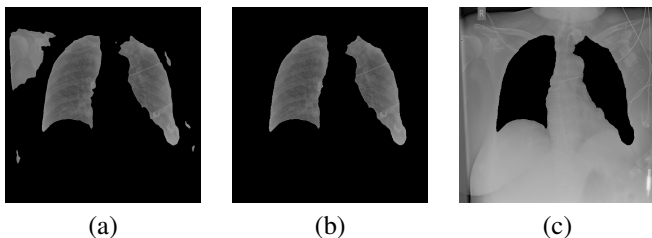


Figure 3: Examples of lung mask obtained using [57] before (a) and after (b) the post-processing step. (c) Example of an inversely-segmented image used, in Section 3.5, to train a model excluding the lung region data (evidence of external confoundig factors).

3 Experimental results

3.1 Dataset and performance metrics

We have used the SIIM-FISABIO-RSNA COVID-19 Detection dataset [49], which is provided by the Society for Imaging Informatics in Medicine (SIIM) and collects CXR images of Covid-19 patients. Images are labeled for the identification and location of pneumonia abnormalities, which are classified into four groups²: *Negative for pneumonia* (28%) images have no lung opacities, *Typical appearance* (47%) are images with presence of bilateral opacities, *Indeterminate appearance* (17%) have unilateral or central opacities, and *Atypical appearance* (8%) are different diseases without features of pneumonia. The SIIM-FISABIO-RSNA training data consists of 6,334 chest scans and is built from two datasets: BIMCV-COVID19+ [45] and MIDRC-RICORD [47].

Original images are in the DICOM format (Digital Imaging and Communication In Medicine) with a resolution over 2K. In our experiments, images have been cropped and resized to a 224×224 resolution, and an 80%-20% train-val split has been used. Performance is assessed in terms of balanced accuracy.

3.2 Curricular SSL training scheme configuration

In our experiments, we have used ResNet-50 [21] architecture for the backbone of the model trained with the scheme described in Section 2. This architecture has been used in several recent works [68, 69] on pneumonia recognition in Covid-19 patients, and shows competitive performance with respect to DenseNet-121 [23]—another common choice for the task [66]. Besides, ResNet-50 is less computational-demanding than DenseNet-121, which allows to perform exhaustive training experiments, as those required for measuring the effectiveness and biases of different combinations of SSL tasks and LR, as the main objective of the experiments is to evaluate the performance gain obtained through curricular SSL pretraining.

Four different SSL pretext tasks, and some of their combinations have been explored, namely: MoCo v2 [10], SwAV [8], Relative Location [16] and Rotation Prediction [9], using the MMSelfSup framework [3]. Table 1 collects the training hyperparameters that are used in each training step. A weighted cross-entropy loss, following class ratios detailed in Subsection 3.1, guides the training process. For every training scheme, and training step, we perform the LR search described in Section 2. The number of epochs for the LR search has been selected, per task, as the minimum number of epochs required to establish an ordering

²A detailed explanation of each label can be found in [49]

Task	Batch Size	LR-Search epochs	LR Range	Full-training epochs	Optimizer	Momentum	Weight decay
Classification	64	80	[0.01-0.25]	150	SGD	0.9	1e-4
Relative Location	32	20	[0.01-0.25]	30	SGD	0.9	1e-4
Rotation Prediction	16	20	[0.01-0.25]	30	SGD	0.9	1e-4
MoCo v2	32	20	[0.01-0.25]	30	SGD	0.9	1e-4
SwAV	8	20	[0.01-0.25]	30	LARS	0.9	1e-4

Table 1: Values of training hyperparameters for the training tasks. Fixed for all experiments.

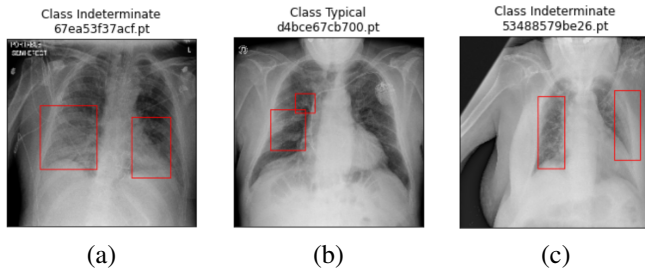


Figure 4: Examples of labeling inconsistencies taken from [56]: (a) bilateral opacity (nominally *Typical*) labeled as *Indeterminate*; (b) unilateral opacity (nominally *Indeterminate*) labeled as *Typical*; (c) bilateral, lower-to-central lung opacity (nominally *Typical*) labeled as *Indeterminate*.

based on performance (which is maintained afterwards). The number of epochs for full-training is selected to ensure training convergence.

As a reference, we compare the SSL-pretrained results with two different baselines: training the classifier from initial random weights (*Scratch*), and training it from *ImageNet* weights (following the same LR search procedure).

3.3 Discussion on the labeling consistency of the SIIM-FISABIO-RSNA COVID-19 Detection dataset

Existing literature indicates that the SIIM-FISABIO-RSNA COVID-19 Detection dataset may present labeling inconsistencies regarding the positions of the opacities [56]. In particular, the annotations often confuse the *Typical* and *Indeterminate* classes, as they both correspond to pneumonia pathologies: i.e., the images labeled as *Typical* have the common symptoms of pneumonia (bilateral opacities), while images labeled as *Indeterminate* correspond to pneumonia but are characterized by uncommon symptoms. Examples of labeling inconsistencies are shown in Figure 4. This inconsistency may be particularly problematic for the *Indeterminate* class, as the number of images (1076) is lower than the *Typical* class (2977). Besides, the *Atypical* class collects all pathological images that do not correspond to pneumonia, thus it may present a high intra-class variation. This, coupled with the shortage of training data belonging to the *Atypical* class (506 images) presents an impediment for an effective learning of class features by the model.

Considering the aforementioned issues, we first evaluate the capability of the CNN architecture to learn effective representations for all classes, and thus to achieve recognition rates beyond random-prediction on all of them. We train the supervised baselines and compare their performance with the SSL-pretrained models, as shown in Table 2. The results indicate that the model is unable to fit the *Indeterminate appearance* and *Atypical appearance*

Pretraining	Negative Acc, %		Typical Acc, %		Indeterminate Acc, %		Atypical Acc, %		Mean Acc, %	
	Train	Validation	Train	Validation	Train	Validation	Train	Validation	Train	Validation
Scratch	85.82	74.36	82.02	67.86	19.60	0.46	25.33	0.99	53.19	35.923
ImageNet	84.24	79.74	85.26	82.13	15.90	6.07	29.50	0.00	53.72	41.988
RelativeLoc	85.86	81.32	83.57	84.75	17.90	0.00	47.80	0.00	58.78	41.521
RotationPred	80.91	81.01	82.04	84.42	8.57	0.00	27.00	0.00	49.63	41.360
SwAV	82.32	77.84	80.61	84.59	9.75	0.00	12.66	0.00	46.33	40.608
MoCo v2	82.56	82.27	82.49	83.60	23.20	1.40	21.33	0.00	52.39	41.822

Table 2: Results of the experiments with one SSL task with the training and validation data.

Curriculum	Pretraining	Validation Acc (%)	AIL (%)
-	ImageNet	82.75	38.16
-	Scratch	83.69	37.30
-	Rel-Loc	83.62	36.33
-	MoCo v2	83.89	37.40
-	Swav	83.97	42.82
-	Rotation	84.72	45.95
✓	MoCo v2 + Rotation	84.77	47.92
	MoCo v2 + Rel-Loc	85.59	39.57
✓	MoCo v2 + SwAV	83.67	41.79
	Rotation + MoCo v2	76.08	31.87
	Rotation + Rel-Loc	84.33	44.48
	Rotation + SwAV	84.81	41.46
✓	Rel-Loc + Rotation	84.54	48.63
✓	Rel-Loc + MoCo v2	82.79	39.41
✓	Rel-Loc + SwAV	85.27	46.26
✓	SwAV + Rotation	83.89	47.16
	SwAV + Rel-Loc	84.92	43.05
	SwAV + MoCo v2	82.37	36.51
	MoCo v2 + Rotation + Rel-Loc	85.28	38.82
	MoCo v2 + Rotation + SwAV	84.80	30.69
	MoCo v2 + Rel-Loc + Rotation	84.19	38.51
	MoCo v2 + Rel-Loc + SwAV	85.49	46.30
✓	MoCo v2 + SwAV + Rotation	85.67	40.19
	MoCo v2 + SwAV + Rel-Loc	83.74	40.89

Table 3: Balanced accuracies and AIL scores for the curricular SSL-task pretraining configurations. Sequential orderings for SSL-tasks read left to right. The curriculum column indicates whether a SSL-task combination follows a curriculum ordering. Results in bold refer to the highest score of each block, while results in blue are the highest scores overall.

classes, not even for training data, yielding lower than random performance. Hereinafter, we restrict our training and evaluation processes to the training and classification of the two majority classes (*Negative* and *Typical*). Thereby, we avoid interferences caused by inconsistently-labeled problems that can lead to results misinterpretations and may occlude the hypothetical benefits of using SSL.

3.4 Performance results for curricular SSL pretrained models

The balanced accuracy performances for models trained with different curricular SSL pretraining configurations on two classes: *Negative* and *Typical*, together with the two baselines—ImageNet, and Scratch, can be found in Table 3. We have tested single-task pretraining, all possible combinations of two-task pretraining, and a subset of combinations of three-task pretraining. The selection of the subset of three-task pretraining combinations is defined according to the results of two-task ones: all two-task combinations ending with MoCo v2 decrease the performance with respect to the single-task alternative, e.g, Rotation Prediction + MoCo v2 presents an accuracy (76.08%) lower than Rotation Prediction (84.72%), and even the baselines. Conversely, MoCo v2 + Relative-Location (which starts with MoCo v2) results in the highest accuracy among all two-task combinations (85.59%). Therefore, we evaluated all possible three-task combinations with MoCo v2 as the first pretraining step.

Performances in Table 3 indicate that there is a significant gap in performance between the baseline models: training from Scratch (83.69%) achieves a better performance than supervised pretraining on ImageNet (82.75%). This may be caused by a large domain gap between a natural imagining dataset (ImageNet) and the target CXR dataset. Among single SSL-tasks pretraining task, Rotation Prediction achieves the best performance (84.72%), outperforming both baselines. Performance is further improved for the best combination of two SSL-tasks (MoCo v2 + Relative Location; 85.59%) and three (MoCo v2 + SwAV + Rotation Prediction; 85.67%). All together, these performances experimentally validate our hypotheses: (i) SSL pretraining benefits performance and (ii) some sequential combinations of SSL tasks further improve performances. However, the performance gain is smaller as additional tasks are included, suggesting that performance may be saturating.

In [14], curricular SSL orderings are defined based on the accuracy achieved by single-SSL task pretraining plus downstream task fine-tuning. The *curriculum* order corresponds to a purely incremental accuracy order. This curriculum premise is fulfilled for the best three-task combination. For two SSL-tasks, the second best option (Relative Location + SwAV: 85.27%) also follows a curriculum order, indicating that arranging the SSL tasks in a curriculum order yields a performance competitive with top-performance combinations.

3.5 Model attention results: AIL score

This section provides a comparison on the degree of attention in the lung region, among the models evaluated in Section 3.4, using the average AIL score described in Section 2.2. The results for all the models, averaged for all validation images, are shown in Table 3, and Figure 5 shows the correlation between the AIL score and accuracy for each model. The results show that 15 out of 21 SSL-pretrained models show an AIL score exceeding that of the ImageNet baseline (38.16%) and accuracy higher than that of the Scratch baseline (83.69%). The figure also demonstrates that the models with a high AIL score, and thus, focus more in the lung area, have a greater performance. These are the models within the area are bounded in the top right corner of Figure 5, yielding top-accuracy values and a high AIL score. This gives an indication that SSL-pretraining may be beneficial to obtain accurate models that show a higher degree of attention in the lung regions, and thus, are more robust to confounding factors in the training dataset, as described in Section 3.3.

Furthermore, there is evidence that multiple-task pretraining increases AIL score, along with accuracy. Regarding single SSL pretraining, the higher AIL score corresponds to Rotation Prediction (45.95%) which also shows the higher single-task accuracy. For combinations

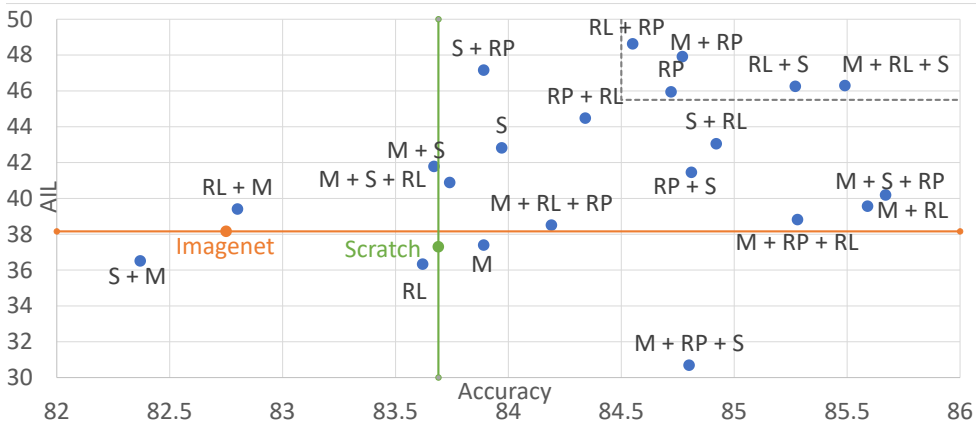


Figure 5: Relation between accuracy and AIL scores for the evaluated models. The green line indicates the best baseline accuracy (Scratch), while the orange indicates the highest baseline AIL score (Imagenet). The labels refer to: MoCo v2 (M), SwAV (S), Relative Location (RL) and Rotation Prediction (RP). For the sake of visualization, the RP+M is removed from the graph (Acc. 76.08%).

of two SSL tasks, the higher AIL score corresponds to Relative Location + Rotation Prediction (48.63%)—the best combination of models among the studied ones. Interestingly, the highest AIL score in each block of two SSL-tasks combinations ends with Rotation Prediction, which also yields the highest AIL score individually. Finally the best combination of 3 SSL tasks is MoCo v2 + Relative Location + SwAV (46.30%).

Experimental verification on the existence of confounding factors Finally, leveraging the lung segmentation strategy, we have performed an additional analysis that corroborates the existence of confounding factors out of the lung regions. Specifically, we have trained the Scratch and ImageNet baselines using inversely-segmented images, i.e, removing the lung regions from the image (an example can be found in Figure 3) achieving a 71.83% and a 75.31% of balanced accuracy respectively. These results are significantly over the 50% threshold that corresponds to a random guess. This result confirms that data outside the lung regions can act as a spurious shortcut (which can be dataset dependent) for the pneumonia classification problem. Thus, models with a higher degree of attention in the lung regions (such as SSL-pretrained ones) may embody models with better generalization capabilities.

4 Conclusions

In this work, we evaluated the performance gain of curricular SSL training scheme for pneumonia classification in CXR images of Covid-19 patients. We show that a combination of SSL tasks can outperform pretraining on ImageNet, or training directly with the target data. With our best configuration, MoCo v2 + SwAV + Relative Location, we achieve a **+1.98%** accuracy increase over the baselines. The results provide evidence that additional SSL tasks can increase the performance of the model compared to pretraining with only one SSL task. Finally, an SSL task ordering based on single-SSL pretraining accuracies (curriculum order)

results which are the best (or close) to all evaluated combinations.

Moreover, we show that curricular SSL pretraining scheme helps to build models that are more robust to the possible existence of confounding factors outside the lung region, which may avoid overfitting to the training dataset and to increase the generalization capabilities of the model. This is assessed by means of a novel attention score (AIL) that captures the level of attention of a model in an image region—lungs in this case. The importance behind creating robust models is to avoid overfitting to the training dataset and to increase the generalization capabilities of the model in other datasets.

References

- [1] Ahmed Afifi, Noor E Hafsa, Mona AS Ali, Abdulaziz Alhumam, and Safa Alsalman. An ensemble of global and local-attention based convolutional neural networks for covid-19 diagnosis on chest x-ray images. *Symmetry*, 13(1):113, 2021.
- [2] Daniel Arias-Garzón, Jesús Alejandro Alzate-Grisales, Simon Orozco-Arias, Harold Brayan Arteaga-Arteaga, Mario Alejandro Bravo-Ortiz, Alejandro Mora-Rubio, Jose Manuel Saborit-Torres, Joaquim Àngel Montell Serrano, Maria de la Iglesia Vayá, Oscar Cardona-Morales, et al. Covid-19 detection in x-ray images using convolutional neural networks. *Machine Learning with Applications*, 6:100138, 2021.
- [3] Moinak Bhattacharya, Shubham Jain, and Prateek Prasanna. Radiotransformer: A cascaded global-focal transformer for visual attention-guided disease classification. *arXiv preprint arXiv:2202.11781*, 2022.
- [4] Erdi Çallı, Ecem Sogancioglu, Bram van Ginneken, Kicky G van Leeuwen, and Keelin Murphy. Deep learning for chest x-ray analysis: A survey. *Medical Image Analysis*, 72:102125, 2021.
- [5] Mathilde Caron, Ishan Misra, Julien Mairal, Priya Goyal, Piotr Bojanowski, and Armand Joulin. Unsupervised learning of visual features by contrasting cluster assignments. *Advances in Neural Information Processing Systems*, 33:9912–9924, 2020.
- [6] Mathilde Caron, Hugo Touvron, Ishan Misra, Hervé Jégou, Julien Mairal, Piotr Bojanowski, and Armand Joulin. Emerging properties in self-supervised vision transformers. In *Proceedings of the IEEE/CVF International Conference on Computer Vision*, pages 9650–9660, 2021.
- [7] Ting Chen, Simon Kornblith, Mohammad Norouzi, and Geoffrey Hinton. A simple framework for contrastive learning of visual representations. In *International conference on machine learning*, pages 1597–1607. PMLR, 2020.
- [8] Ting Chen, Simon Kornblith, Kevin Swersky, Mohammad Norouzi, and Geoffrey E Hinton. Big self-supervised models are strong semi-supervised learners. *Advances in neural information processing systems*, 33:22243–22255, 2020.
- [9] Xinlei Chen and Kaiming He. Exploring simple siamese representation learning. In *Proceedings of the IEEE/CVF Conference on Computer Vision and Pattern Recognition*, pages 15750–15758, 2021.

- [10] Xinlei Chen, Haoqi Fan, Ross Girshick, and Kaiming He. Improved baselines with momentum contrastive learning. *arXiv preprint arXiv:2003.04297*, 2020.
- [11] Xinlei Chen, Saining Xie, and Kaiming He. An empirical study of training self-supervised vision transformers. In *Proceedings of the IEEE/CVF International Conference on Computer Vision*, pages 9640–9649, 2021.
- [12] Noel CF Codella, David Gutman, M Emre Celebi, Brian Helba, Michael A Marchetti, Stephen W Dusza, Aadi Kallou, Konstantinos Liopyris, Nabin Mishra, Harald Kittler, et al. Skin lesion analysis toward melanoma detection: A challenge at the 2017 international symposium on biomedical imaging (isbi), hosted by the international skin imaging collaboration (isic). In *2018 IEEE 15th international symposium on biomedical imaging (ISBI 2018)*, pages 168–172. IEEE, 2018.
- [13] MMSelfSup Contributors. MMSelfSup: Openmmlab self-supervised learning toolbox and benchmark. <https://github.com/open-mmlab/mmselfsup>, 2021.
- [14] Alex J DeGrave, Joseph D Janizek, and Su-In Lee. Ai for radiographic covid-19 detection selects shortcuts over signal. *Nature Machine Intelligence*, 3(7):610–619, 2021.
- [15] Carl Doersch and Andrew Zisserman. Multi-task self-supervised visual learning. In *Proceedings of the IEEE international conference on computer vision*, pages 2051–2060, 2017.
- [16] Carl Doersch, Abhinav Gupta, and Alexei A Efros. Unsupervised visual representation learning by context prediction. In *Proceedings of the IEEE international conference on computer vision*, pages 1422–1430, 2015.
- [17] Mark Everingham, Luc Van Gool, Christopher KI Williams, John Winn, and Andrew Zisserman. The pascal visual object classes (voc) challenge. *International journal of computer vision*, 88(2):303–338, 2010.
- [18] Matej Gazda, Ján Plavka, Jakub Gazda, and Peter Drotar. Self-supervised deep convolutional neural network for chest x-ray classification. *IEEE Access*, 9:151972–151982, 2021.
- [19] Spyros Gidaris, Praveer Singh, and Nikos Komodakis. Unsupervised representation learning by predicting image rotations. *arXiv preprint arXiv:1803.07728*, 2018.
- [20] Jean-Bastien Grill, Florian Strub, Florent Altché, Corentin Tallec, Pierre Richemond, Elena Buchatskaya, Carl Doersch, Bernardo Avila Pires, Zhaohan Guo, Mohammad Gheshlaghi Azar, et al. Bootstrap your own latent—a new approach to self-supervised learning. *Advances in neural information processing systems*, 33:21271–21284, 2020.
- [21] Kaiming He, Xiangyu Zhang, Shaoqing Ren, and Jian Sun. Deep residual learning for image recognition. In *Proceedings of the IEEE conference on computer vision and pattern recognition*, pages 770–778, 2016.
- [22] Kaiming He, Haoqi Fan, Yuxin Wu, Saining Xie, and Ross Girshick. Momentum contrast for unsupervised visual representation learning. In *Proceedings of the IEEE/CVF conference on computer vision and pattern recognition*, pages 9729–9738, 2020.

- [23] Gao Huang, Zhuang Liu, Laurens Van Der Maaten, and Kilian Q Weinberger. Densely connected convolutional networks. In *Proceedings of the IEEE conference on computer vision and pattern recognition*, pages 4700–4708, 2017.
- [24] Stefan Jaeger, Sema Candemir, Sameer Antani, Yi-Xiáng J Wáng, Pu-Xuan Lu, and George Thoma. Two public chest x-ray datasets for computer-aided screening of pulmonary diseases. *Quantitative imaging in medicine and surgery*, 4(6):475, 2014.
- [25] Ashish Jaiswal, Ashwin Ramesh Babu, Mohammad Zaki Zadeh, Debapriya Banerjee, and Fillia Makedon. A survey on contrastive self-supervised learning. *Technologies*, 9(1):2, 2020.
- [26] Kaggle. Aptos 2019 blindness detection, 2019. URL <https://www.kaggle.com/c/aptos2019-blindness-detection/data>.
- [27] Alex Krizhevsky, Ilya Sutskever, and Geoffrey E Hinton. Imagenet classification with deep convolutional neural networks. *Advances in neural information processing systems*, 25, 2012.
- [28] Arkadiusz Kwasigroch, Michał Grochowski, and Agnieszka Mikołajczyk. Self-supervised learning to increase the performance of skin lesion classification. *Electronics*, 9(11):1930, 2020.
- [29] Paras Lakhani, John Mongan, Chinmay Singhal, Quan Zhou, Katherine P Andriole, William F Auffermann, Prasanth Prasanna, Theresa Pham, Michael Peterson, Peter J Bergquist, et al. The 2021 siim-fisabio-rsna machine learning covid-19 challenge: Annotation and standard exam classification of covid-19 chest radiographs. 2021.
- [30] Rebecca Sawyer Lee, Francisco Gimenez, Assaf Hoogi, Kanae Kawai Miyake, Mia Gorovoy, and Daniel L Rubin. A curated mammography data set for use in computer-aided detection and diagnosis research. *Scientific data*, 4(1):1–9, 2017.
- [31] Diana E Litmanovich, Michael Chung, Rachael R Kirkbride, Gregory Kicska, and Jeffrey P Kanne. Review of chest radiograph findings of covid-19 pneumonia and suggested reporting language. *Journal of thoracic imaging*, 35(6):354–360, 2020.
- [32] Shikun Liu, Edward Johns, and Andrew J Davison. End-to-end multi-task learning with attention. In *Proceedings of the IEEE/CVF conference on computer vision and pattern recognition*, pages 1871–1880, 2019.
- [33] Christos Matsoukas, Johan Fredin Haslum, Magnus Söderberg, and Kevin Smith. Is it time to replace cnns with transformers for medical images? *arXiv preprint arXiv:2108.09038*, 2021.
- [34] Mehdi Noroozi and Paolo Favaro. Unsupervised learning of visual representations by solving jigsaw puzzles. In *European conference on computer vision*, pages 69–84. Springer, 2016.
- [35] Junghoon Park, Il-Youp Kwak, and Changwon Lim. A deep learning model with self-supervised learning and attention mechanism for covid-19 diagnosis using chest x-ray images. *Electronics*, 10(16):1996, 2021.

- [36] Muhammad Ridzuan, Ameer Ali Bawazir, Ivo Gollini Navarette, Ibrahim Almakky, and Mohammad Yaqub. Challenges in covid-19 chest x-ray classification: Problematic data or ineffective approaches? *arXiv preprint arXiv:2201.06052*, 2022.
- [37] Raghavendra Selvan, Erik B Dam, Nicki S Detlefsen, Sofus Rischel, Kaining Sheng, Mads Nielsen, and Akshay Pai. Lung segmentation from chest x-rays using variational data imputation. *arXiv preprint arXiv:2005.10052*, 2020.
- [38] Ankita Shelke, Madhura Inamdar, Vruddhi Shah, Amanshu Tiwari, Aafiya Hussain, Talha Chafekar, and Ninad Mehendale. Chest x-ray classification using deep learning for automated covid-19 screening. *SN computer science*, 2(4):1–9, 2021.
- [39] Sadia Showkat and Shaima Qureshi. Efficacy of transfer learning-based resnet models in chest x-ray image classification for detecting covid-19 pneumonia. *Chemometrics and Intelligent Laboratory Systems*, 224:104534, 2022.
- [40] Nathan Silberman, Derek Hoiem, Pushmeet Kohli, and Rob Fergus. Indoor segmentation and support inference from rgb-d images. In *European conference on computer vision*, pages 746–760. Springer, 2012.
- [41] Kirill Sirotkin, Marcos Escudero Viñolo, Pablo Carballeira, and Juan Carlos San-Miguel. Improved skin lesion recognition by a self-supervised curricular deep learning approach. *arXiv preprint arXiv:2112.12086*, 2021.
- [42] Emily B Tsai, Scott Simpson, Matthew P Lungren, Michelle Hershman, Leonid Roshkovan, Errol Colak, Bradley J Erickson, George Shih, Anouk Stein, Jayashree Kalpathy-Cramer, et al. The rsna international covid-19 open radiology database (ricord). *Radiology*, 299(1):E204, 2021.
- [43] Philipp Tschandl, Cliff Rosendahl, and Harald Kittler. The ham10000 dataset, a large collection of multi-source dermatoscopic images of common pigmented skin lesions. *Scientific data*, 5(1):1–9, 2018.
- [44] Grant Van Horn, Oisin Mac Aodha, Yang Song, Yin Cui, Chen Sun, Alex Shepard, Hartwig Adam, Pietro Perona, and Serge Belongie. The inaturalist species classification and detection dataset. In *Proceedings of the IEEE conference on computer vision and pattern recognition*, pages 8769–8778, 2018.
- [45] Maria De La Iglesia Vayá, Jose Manuel Saborit, Joaquim Angel Montell, Antonio Pertusa, Aurelia Bustos, Miguel Cazorla, Joaquin Galant, Xavier Barber, Domingo Orozco-Beltrán, Francisco García-García, et al. Bimcv covid-19+: a large annotated dataset of rx and ct images from covid-19 patients. *arXiv preprint arXiv:2006.01174*, 2020.
- [46] Yude Wang, Jie Zhang, Meina Kan, Shiguang Shan, and Xilin Chen. Self-supervised equivariant attention mechanism for weakly supervised semantic segmentation. In *Proceedings of the IEEE/CVF Conference on Computer Vision and Pattern Recognition*, pages 12275–12284, 2020.
- [47] Ho Yuen Frank Wong, Hiu Yin Sonia Lam, Ambrose Ho-Tung Fong, Siu Ting Leung, Thomas Wing-Yan Chin, Christine Shing Yen Lo, Macy Mei-Sze Lui, Jonan Chun Yin Lee, Keith Wan-Hang Chiu, Tom Chung, et al. Frequency and distribution of chest radiographic findings in covid-19 positive patients. *Radiology*, 2020.

- [48] Bolei Zhou, Agata Lapedriza, Jianxiong Xiao, Antonio Torralba, and Aude Oliva. Learning deep features for scene recognition using places database. *Advances in neural information processing systems*, 27, 2014.
- [49] Bolei Zhou, Aditya Khosla, Agata Lapedriza, Aude Oliva, and Antonio Torralba. Learning deep features for discriminative localization. In *Proceedings of the IEEE conference on computer vision and pattern recognition*, pages 2921–2929, 2016.
- [50] Jiuwen Zhu, Yuexiang Li, and S Kevin Zhou. Aggregative self-supervised feature learning from a limited sample. *arXiv preprint arXiv:2012.07477*, 2020.